Received: 1 March 2019 | Revised: 13 June 2019 | Accepted: 12 October 2019

DOI: 10.1002/ajpa.23957

TECHNICAL NOTE

American Journal of PHYSICAL ANTHROPOLOGY | WILEY

Estimating the *in vivo* location of the talus from external surface landmarks

Steven G. Lautzenheiser[1,2] | Adam D. Sylvester[3] | Patricia Ann Kramer[1,2]

[1]Department of Anthropology, University of Washington, Seattle, Washington

[2]Department of Orthopaedics and Sports Medicine, University of Washington, Seattle, Washington

[3]Center for Functional Anatomy and Evolution, The Johns Hopkins University School of Medicine, Baltimore, Maryland

Correspondence
Steven G. Lautzenheiser, Department of Anthropology, University of Washington, Seattle, WA 98195.
Email: lautzs@uw.edu

Abstract

Objectives: Finite element analysis has gained popularity in anthropological research to connect morphological form to measurable function but requires that loads are applied at appropriate anatomical locations. This is challenging for the ankle because the joint surfaces are not easily determined given their deep anatomical location. While the location of the talonavicular and subtalar joints can be directly determined via medical imaging, regression equations are a common, less invasive method to estimate joint locations from surface anatomy. We propose a regression-based method to locate the in vivo positions of the talonavicular and subtalar joints employing three-dimensional (3D) surface markers, such as those used routinely in gait studies.

Methods: Navicular height was measured on weight-bearing radiographs (WBR) and simulated weight-bearing computed tomography (SWCT) scans to ensure SWCT correctly simulated foot weight-bearing configuration. The location of external foot markers and internal locations of the talonavicular and posterior subtalar joint were measured on each SWCT. Stepwise regression analysis was used to select the external markers that best predicted the three internal locations.

Results: Navicular heights measured on WBR and SWCT scans were not statistically different (p = .44), indicating that SWCTs recreate the weight-bearing position of the foot. The navicular tubercle and medial and lateral malleoli were the best predictors of subtalar and talonavicular joint locations. These palpable anatomical locations explained more variation in internal joint location (r^2 > .79; SEE < 3.0 mm) than other landmarks.

Discussion: This study demonstrates that external palpable landmarks can predict the location of the talonavicular and subtalar joints.

KEYWORDS

foot and ankle kinematics, linear regression, navicular height, subtalar joint, talonavicular joint

1 | INTRODUCTION

Finite element analysis (FEA) is a powerful, flexible, and noninvasive method long used in engineering to estimate variables of interest (e.g., stress and strain) and to compared different structures in complex dynamic and static systems (Rayfield, 2007). Advances in computing power and software capabilities have made FEA more accessible to fields outside engineering, such as biology (Jongerius & Lentink, 2010), anthropology (Püschel & Sellers, 2016), and paleontology (Rayfield et al., 2001). Insights gained from FEA have been used successfully within these fields to connect morphological form to measurable function (Nguyen, Pahr, Gross, Skinner, & Kivell, 2014; Smith et al., 2015; Sylvester & Kramer, 2018; Wang et al., 2012).

Human musculoskeletal anatomy can be idealized as a system of linked rigid bodies (i.e., a kinetic chain), in which body segments (e.g., thigh and leg) are modeled as rigid bodies linked together at joints (e.g., the knee). The nature of the system means that motion of one rigid body affects motion of connected (i.e., linked) bodies, and that forces on one side of a joint (e.g., distal femur) are transferred the other side of the joint (e.g., proximal tibia) (Karandikar & Vargas, 2011). Understanding the kinetic chain assists in locating where loads should be applied at various moments of the gait cycle. Kinetic and kinematics analyses can provide the location of the foot's center of pressure, external marker locations (Figure 1), as well as the ground reaction force. The ground reaction force is transferred to the leg through the bones and joints of the foot using the stiffest path (Wang, Pejhan, Wu, & Telichev, 2016). As the talus is the only bony (i.e., stiffest) connection between the foot and the leg, ground reaction forces generated while walking will travel to the talus through two pathways: through the talonavicular joint, when the ground reaction forces are applied to the forefoot (i.e., during late stance) or through the subtalar joint, when the ground reaction forces are transferred from the hindfoot (i.e., from heel strike to foot flat). During midstance, forces are applied through both joints. Since forces applied to the foot always go through the talus it is likely to be subjected to strong selective pressure and hence could be a key to understanding the evolution of the human foot and ankle (Harcourt-Smith & Aiello, 2004).

A critical component of FEA is ensuring that boundary conditions (e.g., forces) are applied to appropriate locations from a functional and anatomical perspective. In order to apply the forces collected in human motion analyses to an FEM of ankle bones, a method is needed to determine the location of these internal joint surfaces without the use of medical imaging. The exact locations of the talonavicular and posterior subtalar joints can, however, only be determined directly via medical imaging, which is costly, inconvenient for participants, and adds unnecessary complexity to analyses (e.g., converting locations within medical image coordinate system to locations in gait lab coordinate system). The goal of this study is, then, to generate regression equations that use palpable landmarks on the external surface of the foot, like those used in gait studies, to estimate the in vivo location of the talonavicular and the subtalar joints.

2 | MATERIALS AND METHODS

Weight-bearing radiographs (WBR) and simulated weight-bearing computed tomography (SWCT) scans of healthy feet were retrieved for 16 randomly selected adults, eight males and eight females, ages 19–66 years from the database from Harborview Medical Center (Seattle, WA), a Level 1 healthcare facility. WBRs and SWCTs were originally collected for clinical evaluation to rule out the presence of an injury or as comparison views for a contralateral injury (Table S1). Talar dome overlap (Christman, 2003; Montagne, Chevrot, & Galmiche, 1981) was used to classify a lateral radiograph as a true lateral view of the foot.

While imaging techniques, such as computed tomography (CT) scanning, provide the ability to visualize musculoskeletal structures, a major limitation for understanding the position of foot bones from medical images is that they often are not weight bearing. Many clinical orthopedic procedures attempt to simulate weight bearing by using a device that applies a load to the soles of the feet through a stiff plate that mimics the ground (Hirschmann, Pfirrmann, Klammer, Espinosa, & Buck, 2014; Richter, Seidl, Zech, & Hahn, 2014). For this study, navicular height, a reliable estimate of longitudinal arch height (Hawes, Nachbauer, Sovak, & Nigg, 1992; Razeghi & Batt, 2002; Roth, Roth, Jotanovic, & Madarevic, 2013), was compared between SWCT and WBRs to determine if SWCT places the bones of the foot into a weight-bearing position. Result of this analysis (discussed in great detail below) demonstrate that radiographic and CT-based navicular heights are not different, indicating that the weight-bearing position of the bones of the foot is recreated in the SWCTs.

Palpable landmarks on the external surface of the foot, such as those used in gait analysis for the attachment of markers, were simulated by points located on the skin surface (Figure 2) of the SWCT and the 3D locations of these simulated external landmarks were extracted as 3D Cartesian coordinates using OsiriX MD (Osirix Viewer, Geneva, Switzerland). Navicular height was measured on both

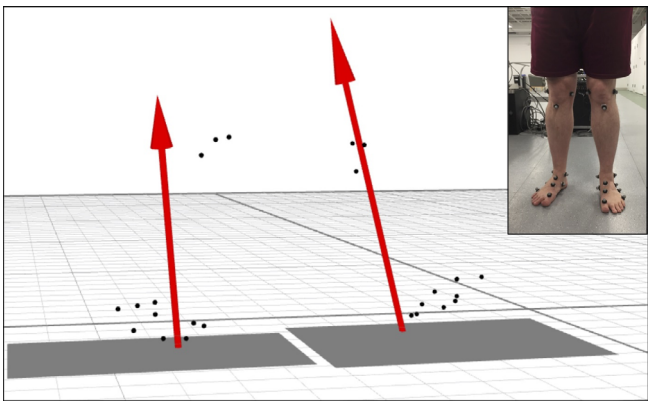

FIGURE 1 Typical gait analysis. Participant with markers and the virtual representation of the participant during a walking trial

FIGURE 2 Simulated external markers placed on the skin on a SWCT representing the dorsal navicular and the center of the second metatarsal head. Markers in image are sized to be visible and are not to scale

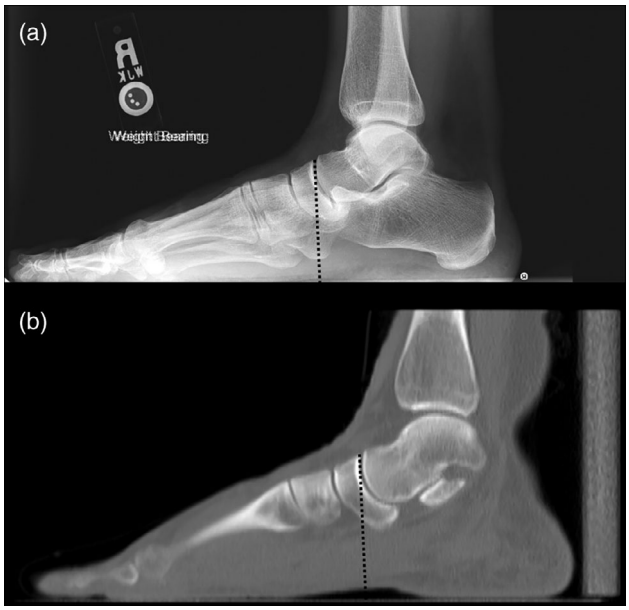

FIGURE 3 Navicular height, represented by the dotted black on weight-bearing radiograph (a) and solid white lines on a SWCT (b), for the same participant

TABLE 1 All landmarks (palpable external and internal points) used measured in this study divided into what computed tomography (CT) slice (sagittal or transverse) was used to measure their location

CT view	Palpable external	Internal point
Sagittal slice	Heel	Center of the talar head
	Dorsal navicular	
	Centers of MT1–MT5 heads	
Transverse slice	Navicular tubercle	Lateral point of the posterior subtalar facet
	Styloid process of the fifth metatarsal	Medial point of the posterior subtalar facet
	Lateral malleolus	Center of the talar head
	Medial malleolus	

lateral WBR and a sagittally oriented slice in the SWCT image stack (Figure 3). The center of each metatarsal head, the dorsal navicular, heel, navicular tubercle, styloid process of the fifth metatarsal, lateral and medial malleoli, lateral and medial point of the posterior subtalar facet (LPST and MPST), and center of the talar head were measured on either sagittal or transverse sliced SWCT (Table 1). A definition for each external landmark is provided in Appendix S1.

The center of the talar head, used to represent the talonavicular joint, was defined as the location where the long axis of the first metatarsal, a line drawn down the longitudinal axis of the shaft of the first metatarsal, intersects the center of the talar head. On all individuals, this position was measured on both sagittal and transverse sliced SWCT stacks. The sagittal slice used was the one in which the most

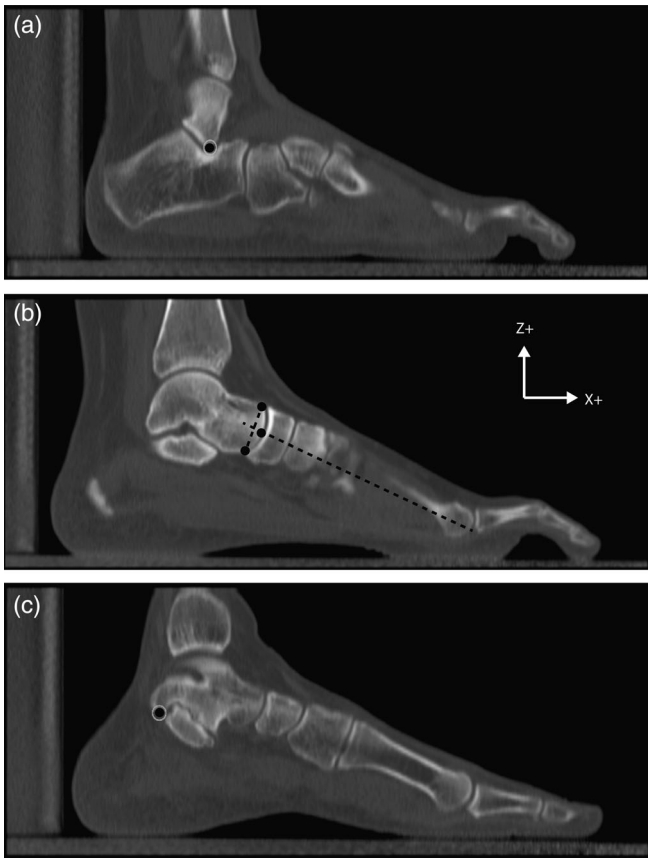

FIGURE 4 Location for the three in vivo talar points on a sagittal sliced SWCT: (a) the lateral posterior subtalar facet, (b) the center of the talar head, and (c) the medial posterior subtalar. Markers in image are not to scale

superior and inferior points of the talar head were visible (Figure 4), while the transverse slice included the most medial and lateral points of the talar head, which were used to determine the center.

To remove variation resulting from foot position during the scan all landmarks of the foot were transformed into a common Cartesian coordinate system. Landmark positions were collected on 11 right and five left feet. Left foot landmarks were reflected in order to create a sample of (pseudo-) right feet. The heel marker was used as the origin for the new foot coordinate system and all landmarks within a foot were translated so that the heel marker was positioned at the origin (0,0,0). Each foot was rotated such that the long axis of the foot was aligned with the *X*-axis. The long axis of the foot was determined by creating a line between the heel marker and the midpoint between first metatarsal and fifth metatarsal markers (Figure 5). In this coordinate system, *X* represents proximodistal, *Y* represents mediolateral, and *Z* represents superioinferior.

Student's *t* tests were conducted to compare navicular height in the SWCT and WBR to determine if SWCT simulates true weight-bearing foot configuration. Some landmarks, such as the LPST and MPST, could only be measured on transverse or sagittal slice SWCT. Student's *t* tests and a multivariate analysis of covariance (MANCOVA) were conducted on the coordinates of the center of the

TABLE 2 Correlations of the navicular tubercle, medial and lateral malleolus to talar joint position

	Talar head						Medial posterior subtalar facet						Lateral posterior subtalar facet					
	X		Y		Z		X		Y		Z		X		Y		Z	
External marker	r^2	*p*-Value	r^2	*p*-Value	r^2	*p*-Value	r^2	*p*-Value	r^2	*p*-Value	r^2	*p*-Value	r^2	*p*-Value	r^2	*p*-Value	r^2	*p*-Value
Navicular tubercle	.79	<.001	.59	<.001	.84	<.001	.53	.001	.45	.004	.64	<.001	.57	.001	.47	.003	.57	.001
Medial malleolus	.65	<.001	.66	<.001	.55	.001	.66	<.001	.56	.001	.64	<.001	.60	<.001	.52	.002	.50	.002
Lateral malleolus	.60	<.001	.54	.001	.53	.001	.48	.003	.47	.003	.55	.001	.74	<.001	.85	<.001	.59	.001

Note: *X* (proximodistal), *Y* (mediolateral), and *Z* (superioinferior) refer to the axes of the foot coordinate system.

FIGURE 5 Virtual reconstruction of the foot from SWCT. The long axis of the foot (black dotted line) is created using the midpoint between markers for the first and fifth metatarsals and the heel. Markers in image are not to scale

TABLE 3 Predictive equations for locating the three talar joints

Predictive equation		r^2	SEE (mm)
Talar head	$X = 23.6 + 0.51 \times$ navicular tubercle (X) $+ 0.48 \times$ lateral malleolus (X)	.91	1.7
	$Y = -14.3 + 0.69 \times$ medial malleolus (Y)	.66	2.3
	$Z = 4.5 + 0.70 \times$ navicular tubercle (Z) $+ 0.30 \times$ lateral malleolus (Z)	.92	1.7
Medial posterior subtalar facet	$X = 1.9 + 0.75 \times$ medial malleolus (X)	.66	1.8
	$Y = -6.0 + 0.57 \times$ medial malleolus (Y)	.56	3.0
	$Z = -5.9 + 0.41 \times$ navicular tubercle(Z) $+ 0.50 \times$ medial malleolus (Z)	.82	2.3
Lateral posterior subtalar facet	$X = 4.9 + 0.68 \times$ lateral malleolus (Y) $+ 0.28 \times$ navicular tubercle (X)	.85	1.9
	$Y = 14.9 + 0.87 \times$ lateral malleolus (Y)	.85	1.5
	$Z = -3.1 + 0.38 \times$ navicular tubercle (Z) $+ 0.36 \times$ lateral malleolus (Z)	.76	1.0

Note: *X* (proximodistal), *Y* (mediolateral), and *Z* (superioinferior) refer to the axes of the foot coordinate system.

talar head for feet in which the position could be measured on both transverse and sagittal slices of the SWCT. This was done to determine if landmarks found only on the transverse slices could be used in the analyses of landmarks found only on sagittal slices. MANCOVA analyses did not indicate differences in measurements, so the analyses are not presented.

Linear regression was used to determine the ability of the locations of the external landmarks to predict the location of the center of the talar head. Stepwise regression was used to determine which external landmarks produced a best fit model for each of the three

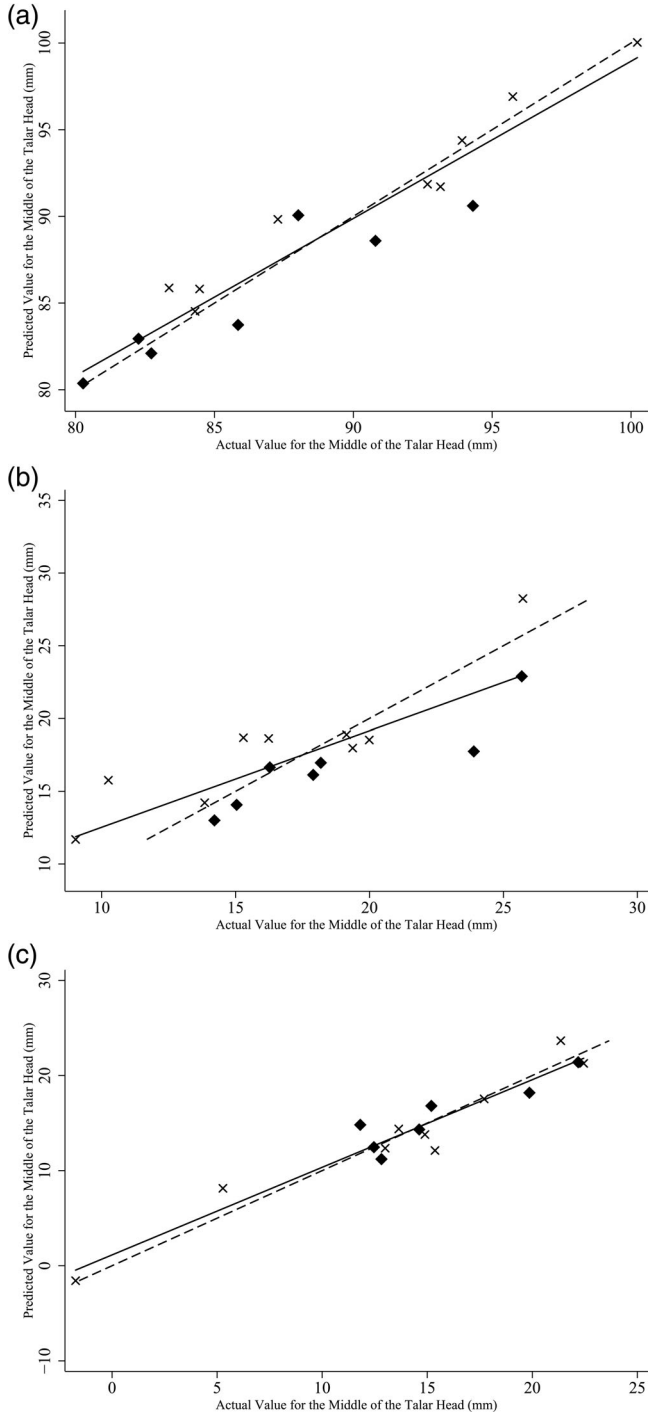

FIGURE 6 The (a) *X*-location, (b) *Y*-location, and (c) *Z*-location in millimeters of the predicted location of the center of the talar head over the measured location of the center of the talar head. Solid line is the best fit line and dotted line is the $y = x$ line. Diamonds are feet that were imaged in order to rule out injury while *X*'s are feet that were imaged as comparison for an injured foot

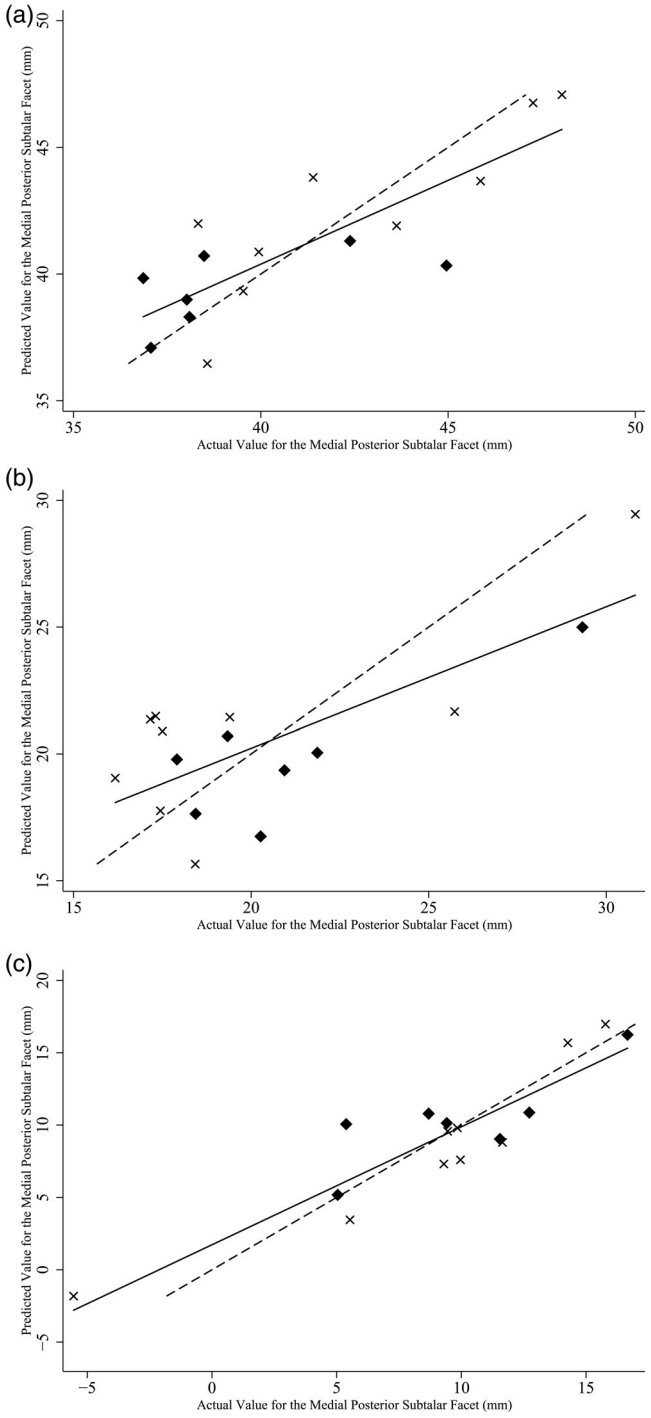

FIGURE 7 The (a) *X*-location, (b) *Y*-location, and (c) *Z*-location in millimeters of the predicted location of the medial posterior subtalar facet over the measured location of the medial posterior subtalar facet. Solid line is the best fit line and dotted line is the $y = x$ line. Diamonds are feet that were imaged in order to rule out injury while *X*'s are feet that were imaged as comparison for an injured foot

talar point's *X*, *Y*, and *Z* coordinates. All statistics were completed in Stata V15 (StataCorp, College Station, TX) using an alpha value of .05. This study was approved by the Institutional Review Board of the University of Washington.

3 | RESULTS

Mean navicular height on WBR is not statistically different ($p = .44$) from that obtained from the SWCT scans: 7.17 cm versus 7.13 cm.

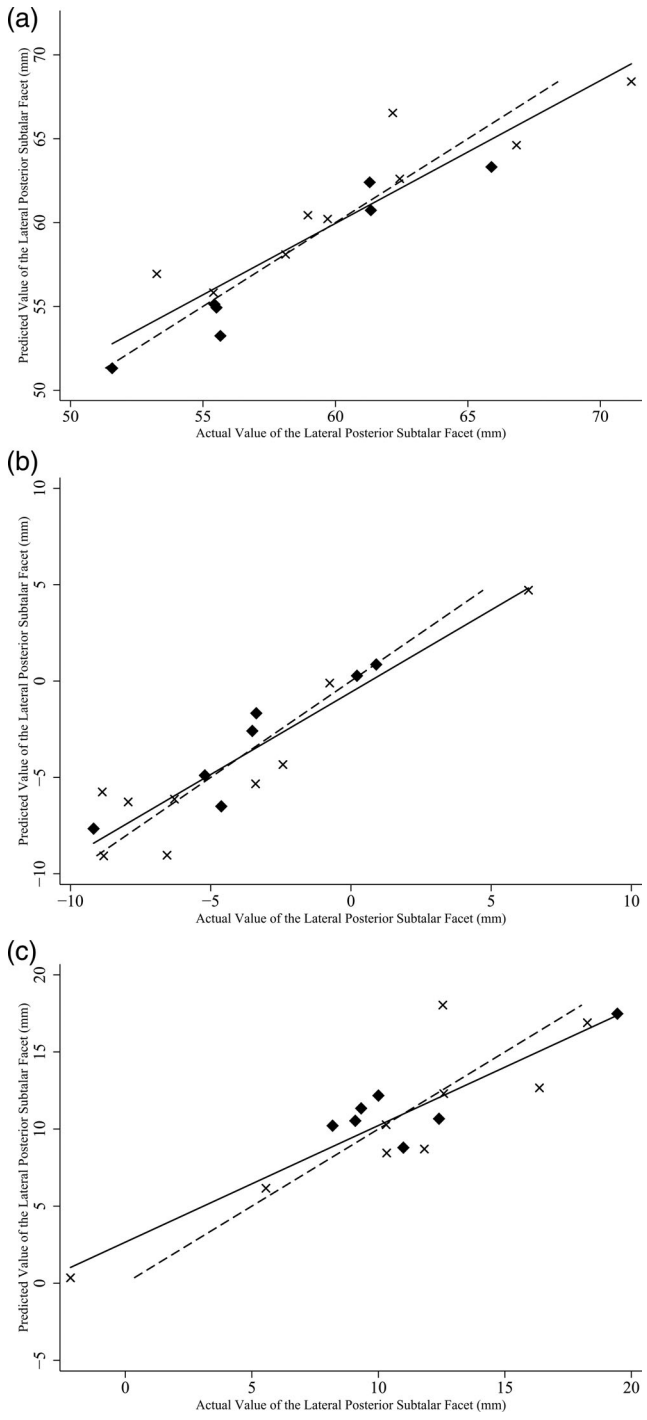

FIGURE 8 The (a) *X*-location, (b) *Y*-location, and (c) *Z*-location in millimeters of the predicted location of the lateral posterior subtalar facet over the measured location of the lateral posterior subtalar facet. Solid line is the best fit line and dotted line is the $y = x$ line. Diamonds are feet that were imaged in order to rule out injury while *X*'s are feet that were imaged as comparison for an injured foot

Mean *X*, *Y*, and *Z* locations of the center of the talar head measured on sagittal SWCT scans are not different from those obtained from transverse SWCT scans in all three coordinates: *X*: 80.04 mm versus 77.27 mm ($p = .70$); *Y*: 26.68 versus 26.35 ($p = .95$); and *Z*: 40.74 versus 42.12 ($p = .89$).

Linear regressions of each landmark's *X*, *Y*, and *Z* coordinates indicated that the lateral and medial malleoli, dorsal navicular, and navicular tubercle are predictive of the center of the talar head and the medial and lateral posterior subtalar points. The centers of the metatarsal heads 2–4 and styloid process of the fifth metatarsal were predictive of only the *X* position of the three internal points and, therefore, were not included in stepwise regression (Tables 2 and S2). The dorsal navicular was not included in the stepwise regression as this point might not be as reliable when the foot rotates about the ankle during the gait cycle due to the movement of the underlying soft tissues.

Stepwise regression revealed that the navicular tubercle and both (lateral and medial) malleoli explained more of the variation of the center of the talar head (r^2 = .66–.92; SEE: 1.7–2.3 mm) and the medial (r^2 = .56–.82; SEE: 2.2–3.2 mm), and lateral (r^2 = 0.76–0.85; SEE: 1.0–1.9 mm) points of posterior subtalar facet than did other external locations (Table 3; Figures 6–8). Adding sex and age to the stepwise regression did not improve the fit of the model.

4 | DISCUSSION

Our results demonstrate that the location of the talonavicular and posterior subtalar joints can be predicted reliably from the location of external markers on the navicular tubercle and lateral and medial malleoli. Due to their close proximity to the talus, it is unsurprisingly that these three bony landmarks were predictive of the location of the joints. The SWCTs used in this study were acquired using conventional medical CT instruments resulting in thicker slice than a high resolution CT. The resolution of the SWCTs could explain why the points for the talonavicular and lateral posterior subtalar joints had higher predictive value compared to the medial posterior subtalar joint. In a living human subject, it is easier to find the center of the talonavicular joint than either of the two subtalar points. Of them, the medial is more difficult than the lateral to identify. Nonetheless, the degree to which variation in internal position of the joints was predicted by external landmarks is encouraging for future FEA of the talus.

Although the feet in this study were unmoving, in gait studies, the foot moves and the position of markers can be affected by the movement of soft tissue, including the skin. An example of this potential problem is the dorsal navicular marker. While a statistically significant predictor of the location of the three joints of interest in this study, the dorsal navicular marker might move more due to skin slippage compared to other markers. The lateral and medial malleoli and navicular tubercle are relatively close to the skin with no intervening tendons, so they have less soft tissue movement. Additionally, they are easily palpable.

The reported regression equations can thus be used to locate the in vivo locations of the talonavicular and posterior subtalar joints using data collected from traditional kinematic gait analyses or clinical examination. While further analyses are required, these same techniques are likely to predict if the in vivo locations of other joints of the foot, such as the calcaneocuboid joint.

ACKNOWLEDGMENTS

We thank the Jerome Debs Chair in Orthopedic Research provided funding for this research and M. Ochoa for helping with the data collection. We also thank our two anonymous reviewers for their feedback.

DATA AVAILABILITY STATEMENT

The data that support the findings of this study are available from the corresponding author upon reasonable request.

ORCID

Steven G. Lautzenheiser https://orcid.org/0000-0001-7999-0702
Adam D. Sylvester https://orcid.org/0000-0002-5234-074X
Patricia Ann Kramer https://orcid.org/0000-0002-6435-9130

REFERENCES

Christman, R. A. (2003). *Foot and ankle radiology*. St. Louis, MO: Churchill Livingstone.

Harcourt-Smith, W. E. H., & Aiello, L. C. (2004). Fossils, feet and the evolution of human bipedal locomotion. *Journal of Anatomy*, *204*(5), 403–416. https://doi.org/10.1111/j.0021-8782.2004.00296.x

Hawes, M. R., Nachbauer, W., Sovak, D., & Nigg, B. M. (1992). Footprint parameters as a measure of arch height. *Foot & Ankle International*, *13*(1), 22–26. https://doi.org/10.1177/107110079201300104

Hirschmann, A., Pfirrmann, C. W. A., Klammer, G., Espinosa, N., & Buck, F. M. (2014). Upright cone CT of the hindfoot: Comparison of the non-weight-bearing with the upright weight-bearing position. *European Radiology*, *24*(3), 553–558. https://doi.org/10.1007/s00330-013-3028-2

Jongerius, S. R., & Lentink, D. (2010). Structural analysis of a dragonfly wing. *Experimental Mechanics*, *50*(9), 1323–1334. https://doi.org/10.1007/s11340-010-9411-x

Karandikar, N., & Vargas, O. O. (2011). Kinetic chains: A review of the concept and its clinical applications. *PM&R*, *3*(8), 739–745. https://doi.org/10.1016/j.pmrj.2011.02.021

Montagne, J., Chevrot, A., & Galmiche, J.-M. (1981). *Atlas of foot radiology*. New York, NY: Masson.

Nguyen, N. H., Pahr, D. H., Gross, T., Skinner, M. M., & Kivell, T. L. (2014). Micro-finite element (μFE) modeling of the siamang (*Symphalangus syndactylus*) third proximal phalanx: The functional role of curvature and the flexor sheath ridge. *Journal of Human Evolution*, *67*, 60–75. https://doi.org/10.1016/j.jhevol.2013.12.008

Püschel, T. A., & Sellers, W. I. (2016). Standing on the shoulders of apes: Analyzing the form and function of the hominoid scapula using geometric morphometrics and finite element analysis. *American Journal of Physical Anthropology*, *159*(2), 325–341. https://doi.org/10.1002/ajpa.22882

Rayfield, E. J., Norman, D. B., Horner, C. C., Horner, J. R., Smith, P. M., Thomason, J. J., & Upchurch, P. (2001). Cranial design and function in a large theropod dinosaur. *Nature*, *409*(6823), 1033–1037. https://doi.org/10.1038/35059070

Rayfield, E. J. (2007). Finite element analysis and understanding the biomechanics and evolution of living and fossil organisms. *Annual Review of Earth and Planetary Sciences 35*(1), 541–576.

Razeghi, M., & Batt, M. E. (2002). Foot type classification: A critical review of current methods. *Gait & Posture*, *15*(3), 282–291. https://doi.org/10.1016/S0966-6362(01)00151-5

Richter, M., Seidl, B., Zech, S., & Hahn, S. (2014). PedCAT for 3D-imaging in standing position allows for more accurate bone position (angle) measurement than radiographs or CT. *Foot and Ankle Surgery*, *20*(3), 201–207. https://doi.org/10.1016/j.fas.2014.04.004

Roth, S., Roth, A., Jotanovic, Z., & Madarevic, T. (2013). Navicular index for differentiation of flatfoot from normal foot. *International Orthopaedics*, *37*(6), 1107–1112. https://doi.org/10.1007/s00264-013-1885-6

Smith, A. L., Benazzi, S., Ledogar, J. A., Tamvada, K., Pryor Smith, L. C., Weber, G. W., … Strait, D. S. (2015). Biomechanical implications of intraspecific shape variation in chimpanzee crania: Moving toward an integration of geometric morphometrics and finite element analysis. *The Anatomical Record*, *298*(1), 122–144. https://doi.org/10.1002/ar.23074

Sylvester, A. D., & Kramer, P. A. (2018). Young's modulus and load complexity: Modeling their effects on proximal femur strain. *The Anatomical Record*, *301*(7), 1189–1202. https://doi.org/10.1002/ar.23796

Wang, Q., Pejhan, K., Wu, C. Q., & Telichev, I. (2016). Load transfer index for composite materials. Mechanics of solids, structures and fluids, Vol. 9, V009T12A009. Houston, Texas, USA: International Mechanical Engineering Congress and Exposition. https://doi.org/10.1115/imece2015-51176

Wang, Q., Wood, S. A., Grosse, I. R., Ross, C. F., Zapata, U., Byron, C. D., … Strait, D. S. (2012). The role of the sutures in biomechanical dynamic simulation of a macaque cranial finite element model: Implications for the evolution of craniofacial form. *The Anatomical Record*, *295*(2), 278–288. https://doi.org/10.1002/ar.21532

SUPPORTING INFORMATION

Additional supporting information may be found online in the Supporting Information section at the end of this article.

How to cite this article: Lautzenheiser SG, Sylvester AD, Kramer PA. Estimating the *in vivo* location of the talus from external surface landmarks. *Am J Phys Anthropol*. 2020;171:354–360. https://doi.org/10.1002/ajpa.23957